An enriched shell element formulation for efficient modeling of multiple delamination propagation in laminates

Jim Brouzoulis[a], Martin Fagerström[a,*]

[a]*Department of Applied Mechanics*
Division on Material and Computational Mechanics
Chalmers University of Technology, Gothenburg, Sweden

Abstract

In the modeling of progressive damage in fiber reinforced polymers, the kinematical representation of delamination is normally treated in one of two ways. Either efficient or accurate modeling of delamination is considered. In the first case, delamination is disregarded or implicitly included in the material modeling. In the second case, delamination is explicitly modeled at a significant numerical cost where all plies are represented by separate elements in the thickness direction, connected by interlaminar cohesive zone elements. In this paper, we therefore aim to take one step closer to more efficient FE analyses by presenting a modeling concept which supports laminate failure analyses requiring only one shell element through the thickness. With this concept, arbitrary delamination propagation is accounted for only in areas where it is needed. In addition, by using this concept, the model preparation time is reduced. We show that the current shell formulation proposed can be utilized to accurately simulate propagating delamination cracks as well as to accurately describe the kinematics of a laminate containing multiple delaminations through the thickness. Thus, we see significant potential for this modeling concept in analyses in which computationally efficiency is of major importance, such as for large scale crash analyses.

Keywords: multiple delamination, XFEM, computational efficiency, shells

*Corresponding author. Address: Hörsalsvägen 7, SE–412 96 Göteborg, Sweden. E-mail:martin.fagerstrom@chalmers.se. Phone: +46 31 772 1300.

1. Introduction

To meet the sharpening targets from regulatory bodies[1] on CO_2 emissions from cars, the automotive industry is currently very active in reducing vehicle weight, where one significant step is to increase the amount of Fibre Reinforced Polymers (FRPs) due to their superior specific properties (*e.g.* specific strength and specific energy absorption in axial crushing) compared to conventional metals. The superior energy absorption capability of FRPs has been analyzed experimentally by many authors, cf. *e.g.* the reviews by Carruthers *et al.* [1] and Jacob *et al.* [2]. From these studies, it can be concluded that for Carbon Fibre Reinforced Polymers (CFRPs) the specific energy absorption in axial compression can be higher or significantly higher compared to aluminium and steel grades used in crash structures today, cf. *e.g.* Hamada *et al.* [3]. Furthermore, it has been shown, cf. Hull [4] and Grauers *et al.* [5], that this beneficial material characteristic is the consequence of a very complicated fracture process in the material involving many competing failure mechanisms, *e.g.* fiber kinking (and breaking) in compression, compressive matrix failure and significant (mixed-mode) delamination. Interestingly, it can be concluded from the paper by Grauers *et al.* that delamination is one of the governing failure mechanisms. Not as a primary energy absorbing mechanism but definitively in the sense that propagating delaminations significantly influence the overall deformation pattern and thereby, indirectly, the occurrence of the other failure mechanisms. From these observations, it is clear that to achieve accurate predictions of the crashworthiness performance of FRP components in simulations – which is an absolute requirement in the automotive development process today if these materials are to be used – the delamination process needs to be explicitly accounted for in an accurate way.

In addition to accuracy, computational efficiency of the structural Finite Element (FE) analysis is equally important to facilitate full scale crash simulations. Thereby, an efficient approximation and solution method for the modeling of propagating delamination cracks is absolutely crucial to meet

[1] As an example, within the European Union new legislations setting mandatory emission reduction targets for new cars are enforced by the European Commission. According to these reduction targets, the fleet average to be achieved by all new cars is 95g/km by 2021, corresponding to a reduction of 40% compared with the 2007 fleet average of 158.7g/km.

today's requirements on virtual development lead times in the automotive industry. Up until now, there have been two variants of how to account for delamination progression in crash (or crush) applications reported in the literature, focusing on *either* efficiency *or* accuracy. With efficiency in focus, shell models with one element through the thickness are used where the delamination propagation is implicitly accounted for by using phenomenological material models which are not based on the physical mechanisms but rather mimicking the total failure process including effects of delamination, cf. *e.g.* Feraboli [6]. In contrast, with more focus on the accuracy, laminates are modeled with many elements through the thickness (possibly one per ply) connected by cohesive interface elements or similar, cf. Bussadori *et al.* [7] and Greve and Pickett [8], although with the obvious drawback of increased numerical cost. In this paper, we therefore aim to take one step closer to more efficient FE analyses, while maintaining good accuracy, by presenting a modeling concept which supports laminate failure analyses requiring only one shell element through the thickness, and where arbitrary delamination propagation is accounted for only in areas where it is needed.

The modeling concept we propose is based on the eXtended Finite Element Method (XFEM) [9, 10] which allows for mesh independent representations of discontinuities (*e.g.* cracks and delaminations) by introducing kinematical enrichments locally in the vicinity of the propagating crack(s). Several researchers before us have successfully utilized the XFEM framework to model failure propagation in composites, cf. *e.g.* Van der Meer *et al.* [11] modeling matrix cracks and delaminations by combining XFEM enhanced solid elements (matrix cracks) and interconnecting classical cohesive elements (delaminations), Ahmed *et al.* [12] proposing a geometrically nonlinear discontinuous solid-like shell element for the modeling of intralaminar crack propagation in thin shell structures and Larsson [13] and de Borst and Remmers [14] modeling arbitrarily located single delaminations. In fact, the currently proposed modeling concept is an extension of the works in [13, 14], with similarities also to the method proposed for modeling two delamination cracks in beams by Batra and Xiao [15]. However, in contrast to the above mentioned works, the current modeling concept allows not only one but arbitrarily many delaminations to be included in one and the same shell. As a consequence, a structural model of a thinwalled laminate can, by using this modeling concept, initially be built up by a single layer of shell elements through the thickness. During loading, the model is then dynamically enriched in critical areas where delamination is predicted. This means that

a significant reduction of total degrees of freedom of the model needed to describe a potentially very complex state of deformation can be achieved, compared to the case where each ply is to be modeled by separate elements (shells or solids) connected by cohesive elements. Thereby, the computational cost is reduced since the total number of degrees of freedom are kept to a minimum.

In the numerical section of this paper we show that the current shell formulation proposed can be utilized to accurately simulate propagating delamination cracks in both mode I and mode II situations. Moreover, we also show that the formulation accurately describes the kinematics of a laminate containing multiple delaminations through the thickness with different sizes. These results thereby indicates that the level of detail in the present approach is such that individual delaminations can be analyzed accurately where present. Moreover, the level of detail (and computational cost) of the model is only increased in areas where delamination actually occurs thereby reducing the computational effort required in large scale analyses. Thus, we foresee the use of this modeling concept in analyses in which computationally efficiency is of major importance.

2. Initial and deformed shell geometry in terms of convected coordinates

As described in the introduction, the primary focus of the current paper is to propose a modeling concept which kinematically can represent arbitrarily many delaminations. We start by presenting the kinematical shell framework which has been considered in the developments of the current modeling concept. The framework consists of three interrelated domains; the inertial Cartesian domain $\mathcal{B}_C$, the undeformed (reference) domain $\mathcal{B}_0$ and the deformed (current) domain $\mathcal{B}$ with pertinent mappings, cf. Figure 1.

As a staring point, the reference configuration $\mathcal{B}_0$ of the shell is considered parameterized is in terms of convected (co-variant) coordinates $\boldsymbol{\xi}$ as

$$\mathcal{B}_0 = \{\boldsymbol{X} := \boldsymbol{\Phi}(\boldsymbol{\xi})\}\,, \tag{1}$$

where we introduced the contracted notation $\boldsymbol{\xi} = (\xi^1, \xi^2, \xi^3 = \xi)$ and $\bar{\boldsymbol{\xi}} = (\xi^1, \xi^2)$ for a point in the shell and on the mid-surface respectively[2]. Further-

[2]To avoid confusion, we will from here on only use $\bar{\boldsymbol{\xi}}$ to denote the in-plane coordinates

more, the outer boundary of the domains are denoted as Ω with an appropriate subscript depending on configuration. As can be seen from Eq. (1), the mapping $\boldsymbol{\Phi}(\boldsymbol{\xi}) \in \mathcal{B}_0$ maps a point $\boldsymbol{\xi}$ in the inertial Cartesian domain to the corresponding point $\boldsymbol{X}$ in the undeformed reference domain. Associated with the mapping $\boldsymbol{\Phi}$, we also have that the co-variant base vectors $\boldsymbol{G}_i$ in the reference domain are expressed in a general sense as

$$\boldsymbol{G}_i = \boldsymbol{\Phi}_{,i}, \tag{2}$$

where $\bullet_{,i}$ denotes the partial derivative of $\bullet$ with respect to $\xi^i,\ i = 1, 2, 3$.

In a similar fashion, the deformed geometry is described by the deformation map $\boldsymbol{\varphi}(\boldsymbol{\xi}) \in \mathcal{B}$ from the inertial Cartesian frame as

$$\mathcal{B} = \{\boldsymbol{x} := \boldsymbol{\varphi}(\boldsymbol{\xi})\}. \tag{3}$$

The pertinent co-variant base vectors in the deformed domain thereby becomes

$$\boldsymbol{g}_i = \boldsymbol{\varphi}_{,i}. \tag{4}$$

Associated with the deformation from the undeformed to the deformed configuration, we obtain the deformation gradient $\boldsymbol{F}$ as

$$\boldsymbol{F} = \boldsymbol{x} \otimes \boldsymbol{\nabla}_{\mathrm{X}} = \boldsymbol{g}_i \otimes \boldsymbol{G}^i, \quad i = 1, 2, 3 \tag{5}$$

where we have also introduced the contra-variant base vectors $\boldsymbol{G}^i = \partial \xi^i / \partial \boldsymbol{X}$ in the reference configuration which are obtained (in a standard manner) as

$$\boldsymbol{G}^i = G^{-1}_{ij} \boldsymbol{G}_j \tag{6}$$

using the metric tensor $G_{ij} = \boldsymbol{G}_i \cdot \boldsymbol{G}_j$.

3. A concept for modeling multiple delaminations in shells

To describe multiple delaminations within one and the same shell element, the above defined deformation maps need to be extended to allow for displacement discontinuities across delamination interfaces. To do so, we propose to locally enrich the displacement approximation of the shell in the vicinity of interlaminar cracks in line with the XFEM, cf. Subsection 3.2 below. However, as a basis for this extension of the deformation maps, we first discuss the geometric description of interlaminar cracks in this context.

---

and ξ to denote the out of plane coordinate. As a consequence, any appearance of *e.g.* ξ^2 should be interpreted as $(\xi^3)^2$

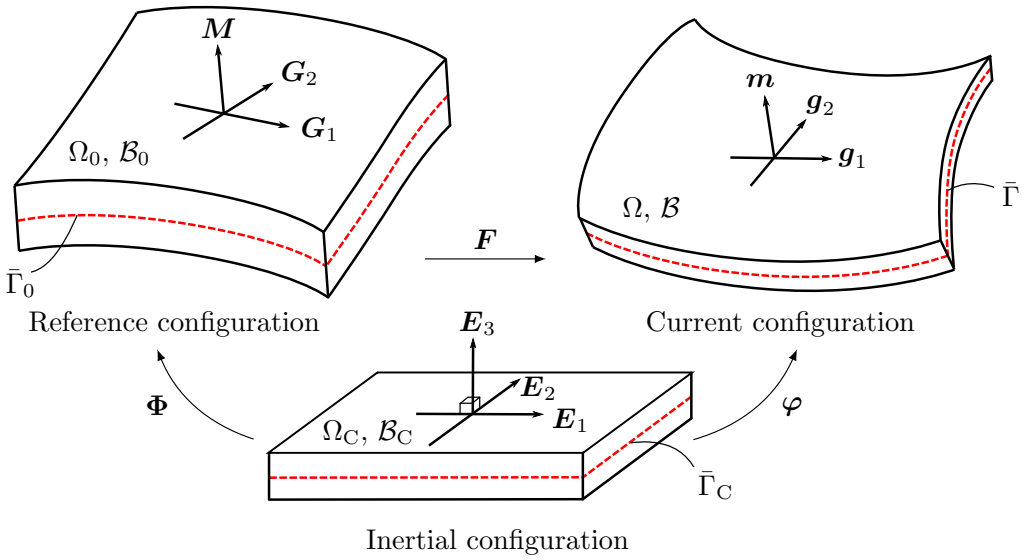

Figure 1: Mappings of shell model defining undeformed and deformed shell configurations relative to the inertial Cartesian frame.

3.1. Geometric description of interlaminar cracks using level sets

Consider a laminate built up from a number of plies, each defined by lying at a constant distance from the mid-surface. Let this laminate contain $\mathrm{N}_{\mathrm{del}}$ delamination surfaces, where Γ_k represents such a surface in the reference configuration, with $k = 1, \ldots \mathrm{N}_{\mathrm{del}}$, cf. Figure 2. Each delamination surface (interlaminar crack) is defined through two level set functions $S_k^{\xi}(\xi)$ and $S_k^{\gamma}(\bar{\boldsymbol{\xi}})$ defined in $\mathcal{B}_C$, where $S_k^{\xi}(\xi) = 0$ defines the position $\bar{\xi}_k$ of the surface in the thickness direction and where $S_k^{\gamma}(\bar{\boldsymbol{\xi}}) = 0$ defines the in-plane crack front – corresponding to $\partial\Gamma_k$ in the reference configuration – of each respective interlaminar crack. Furthermore, to facilitate the deformation map extension presented in the next subsection, both level set functions are defined as mutually orthogonal signed distance functions.

To be specific, the thickness level set $S_k^{\xi}(\xi)$ is the signed distance function to the delamination interface number k, which due to the fact that we consider equidistant plies from the mid-surface can be defined simply as

$$S_k^{\xi} = \xi - \bar{\xi}_k. \tag{7}$$

For later use, we also note that the material gradient of this level set function corresponds exactly to the third contra-variant base vector in the undeformed

configuration

$$S_k^{\xi}\big(\xi(\boldsymbol{X})\big) \otimes \boldsymbol{\nabla}_{\mathrm{X}} = S_{k,i}^{\xi}\boldsymbol{G}^i = \boldsymbol{G}^3, \tag{8}$$

which for most shell theories is identical to the mid-surface normal $\boldsymbol{N}$, cf. also Section 6.

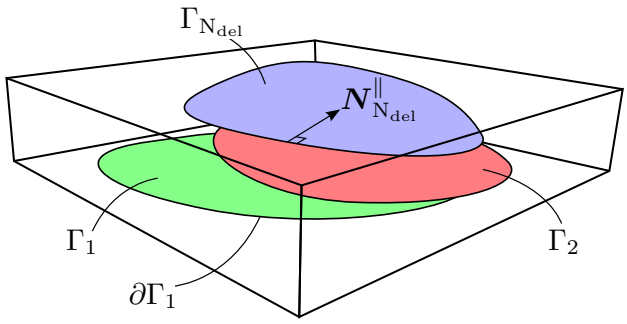

Figure 2: Definition of delamination surfaces with different in-plane extensions. The figure also illustrates the boundary $\partial\Gamma_1$ of the first delamination surface and the binormal $\boldsymbol{N}^{\parallel}_{\mathrm{N_{del}}}$ of the last delamination surface.

As for the in-plane level set $S_k^{\gamma}(\bar{\boldsymbol{\xi}})$, it is defined as the signed distance to the closest point on the boundary $\partial\Gamma_k$ enclosing the delamination surface Γ_k and it is positive inside the zone. By definition, it may then be shown that the material gradient of this level set function becomes

$$S_k^{\gamma}(\bar{\boldsymbol{\xi}}) \otimes \boldsymbol{\nabla}_{\mathrm{X}} = \boldsymbol{N}^{\parallel}_k, \tag{9}$$

where $\boldsymbol{N}^{\parallel}_k$ is defined as the binormal to $\partial\Gamma_k$ pointing into Γ_k, cf. Figure 2.

3.2. Discontinuity enhanced shell kinematics using the XFEM

As discussed above, we seek a formulation that allows for (dis)placement discontinuities across each delamination interface to represent the cracks. For this purpose, we propose a general kinematical extension in line with the XFEM such that the deformation map of the deformed configuration is subdivided into one continuous and one discontinuous part as

$$\boldsymbol{\varphi}(\boldsymbol{\xi}) = \boldsymbol{\varphi}^{\mathrm{c}}(\boldsymbol{\xi}) + \boldsymbol{\varphi}^{\mathrm{d}}(\boldsymbol{\xi}), \tag{10}$$

where the continuous part takes on the same form as the underlying shell formulation, *i.e.* $\boldsymbol{\varphi}$ is replace by $\boldsymbol{\varphi}^{\mathrm{c}}$. For a description using a specific shell formulation, see Section 6.

As for the discontinuous part $\boldsymbol{\varphi}^{\mathrm{d}}$, it is constructed as a sum of enrichments $\boldsymbol{\varphi}_k^{\mathrm{d}}(\boldsymbol{\xi})$ (one for each delamination) following Reference [16] as

$$\boldsymbol{\varphi}^{\mathrm{d}} = \sum_{k=1}^{\mathrm{N_{del}}} \psi_k \boldsymbol{\varphi}_k^{\mathrm{d}} \tag{11}$$

where the existing delamination cracks are numbered globally starting from the bottom of the laminate. In Eq. (11), we have introduced a discontinuous enrichment function ψ_k which in turn is defined as a product between two enrichment functions – one associated with the thickness direction ψ_k^{ξ} and one associated with the tangent plane ψ_k^{γ} – defined as

$$\psi_k^{\xi} = \mathcal{H}\left(S_k^{\xi}\right) \quad \text{and} \quad \psi_k(\boldsymbol{\xi}) = \psi_k^{\xi}(\xi) \cdot \psi_k^{\gamma}(\bar{\boldsymbol{\xi}}) \tag{12}$$

with

$$\psi_k^{\gamma} = \mathcal{H}\left(S_k^{\gamma}\right) \tag{13}$$

where $\mathcal{H}$ is the Heaviside function. Thus, ψ_k^{ξ} takes the form of a step function from delamination crack k and upwards, as illustrated in Figure 3b, and as a consequence to this particular choice of enrichment, the different enrichments couple to each other, cf. Figure 3c. In addition, the enrichment function ψ_k^{γ} ensures that the particular enrichment $\boldsymbol{\varphi}_k^{\mathrm{d}}$ is introduced only for points inside the delamination zone, i.e. only for in-plane positions $\boldsymbol{\Phi}(\bar{\boldsymbol{\xi}}) \in \Gamma_k$. However, please note that, since a Heaviside function is used for the enrichment, the continuity requirement

$$\boldsymbol{\varphi}_k^{\mathrm{d}} = \mathbf{0} \text{ on } \partial\Gamma_k \tag{14}$$

needs to be explicitly enforced.

3.2.1. The discontinuity enhanced deformation gradient

Given the described enrichment of the deformation map presented above, we have what is needed to derive a shell element formulation that can handle multiple delaminations in one and the same element, which is done for a specialized case in Section 6. The procedure however requires the explicit expression for the deformation gradient $\boldsymbol{F}$ associated with the proposed kinematical representation.

To arrive at the explicit expression for $\boldsymbol{F}$, we start by noting that the deformation gradient is established based on the extended kinematics taking

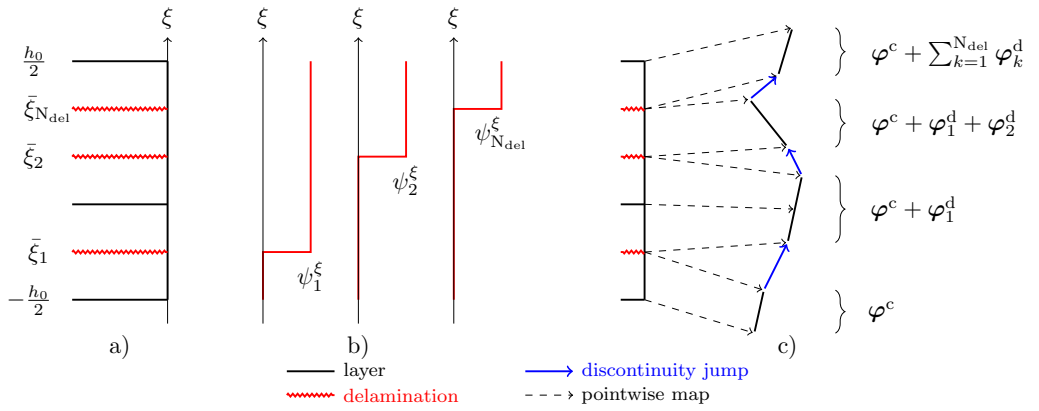

Figure 3: a) Depicts a laminate (of thickness h_0) with several delaminations. b) shows the enrichment functions ψ_k^ξ associated with the thickness direction and c) illustrates the coupling of the discontinuous placement maps.

the following general form:

$$\boldsymbol{F} = \left(\boldsymbol{\varphi}^{\mathrm{c}} + \boldsymbol{\varphi}^{\mathrm{d}}\right) \otimes \boldsymbol{\nabla}_{\mathrm{X}} = \boldsymbol{F}^{\mathrm{b}} + \sum_{k=1}^{\mathrm{N_{del}}} \boldsymbol{F}_{k\psi}^{\mathrm{d}} \tag{15}$$

where $\boldsymbol{F}$ is split into the bounded term $\boldsymbol{F}^{\mathrm{b}}$ and a set of unbounded terms $\{\boldsymbol{F}_{k\psi}^{\mathrm{d}}\}$ where

$$\boldsymbol{F}^{\mathrm{b}} = \boldsymbol{F}^{\mathrm{c}} + \sum_{k=1}^{\mathrm{N_{del}}} \psi_k \boldsymbol{F}_k^{\mathrm{d}} = \boldsymbol{g}_i^{\mathrm{b}} \otimes \boldsymbol{G}^i \tag{16}$$

with $\boldsymbol{F}_k^{\mathrm{d}} = \boldsymbol{\nabla}_{\mathrm{X}} \otimes \boldsymbol{\varphi}_k^{\mathrm{d}}$ and where the corresponding (bounded) spatial covariant base vectors $\boldsymbol{g}_i^{\mathrm{b}}$ are defined as

$$\boldsymbol{g}_i^{\mathrm{b}} = \boldsymbol{g}_i^{\mathrm{c}} + \sum_{k=1}^{\mathrm{N_{del}}} \psi_k \boldsymbol{g}_{ki}^{\mathrm{d}}. \tag{17}$$

These are in turn constructed from the base vectors associated with the continuous and discontinuous deformation maps

$$\boldsymbol{g}_i^{\mathrm{c}} = \boldsymbol{\varphi}_{,i}^{\mathrm{c}}, \tag{18}$$

$$\boldsymbol{g}_{ki}^{\mathrm{d}} = \boldsymbol{\varphi}_{k,i}^{\mathrm{d}}. \tag{19}$$

In Eq. (15), additional terms arise in the expression for the deformation gradient due to the enrichment functions ψ_k. These additional terms can be written as

$$\begin{aligned}\boldsymbol{F}^{\mathrm{d}}_{k\psi} &= \boldsymbol{\varphi}^{\mathrm{d}}_k \otimes \boldsymbol{\nabla}_{\mathrm{X}}\, \psi_k \\ &= \boldsymbol{\varphi}^{\mathrm{d}}_k \otimes \psi^{\gamma}_k \frac{\partial \mathcal{H}\left(S^{\xi}_k\right)}{\partial S^{\xi}_k} \boldsymbol{G}^3 + \psi^{\xi}_k \underbrace{\boldsymbol{\varphi}^{\mathrm{d}}_k \otimes \boldsymbol{\nabla}_{\mathrm{X}}\, \psi^{\gamma}_k}_{=\boldsymbol{0}} \\ &= \psi^{\gamma}_k \delta^{\xi}_k \boldsymbol{\varphi}^{\mathrm{d}}_k \otimes \boldsymbol{G}^3 = \delta^{\xi}_k \psi^{\gamma}_k [\![\boldsymbol{\varphi}]\!]_k \otimes \boldsymbol{G}^3,\end{aligned} \tag{20}$$

by introducing the (dis)placement jump across Γ_k as

$$[\![\boldsymbol{\varphi}]\!]_k = \boldsymbol{\varphi}^{\mathrm{d}}_k. \tag{21}$$

Furthermore, in the derivations above we used the results from Eqs. (8) and (9) and the fact that

$$\frac{\partial S^{\xi}_k}{\partial \xi} = 1 \text{ and } \frac{\partial\, \mathcal{H}(S^{\xi}_k)}{\partial\, S^{\xi}_k} = \delta^{\xi}_k \tag{22}$$

where δ^{ξ}_k is a Dirac delta function with the property that

$$\int_{\mathcal{B}_0} \psi^{\gamma}_k \delta^{\xi}_k \bullet \, \mathrm{d}\mathcal{B}_0 = \int_{\Gamma_k} \bullet \, \mathrm{d}\Gamma_k \tag{23}$$

In addition, it is in Eq. (20) indicated that

$$\boldsymbol{\varphi}^{\mathrm{d}}_k \otimes \boldsymbol{\nabla}_{\mathrm{X}}\, \psi^{\gamma}_k = \boldsymbol{0} \tag{24}$$

which can be shown to be a direct consequence of the continuity requirement for $\boldsymbol{\varphi}^{\mathrm{d}}_k$ on $\partial\Gamma_k$ introduced above, cf. Eq. (14).

4. Weak form of momentum balance

In this section, we establish the momentum balance in a weak setting based on the described kinematics. We start from the basic weak form of the momentum balance in terms of contributions from inertia $\mathcal{W}^{\mathrm{ine}}$, internal work $\mathcal{W}^{\mathrm{int}}$ and external work $\mathcal{W}^{\mathrm{ext}}$ such that the problem can be stated as

Find: $\boldsymbol{\varphi} \in \mathcal{V}$

$$\mathcal{W}^{\mathrm{ine}}\left(\ddot{\boldsymbol{\varphi}}; \delta\boldsymbol{\varphi}\right) + \mathcal{W}^{\mathrm{int}}\left(\boldsymbol{\varphi}; \delta\boldsymbol{\varphi}\right) = \mathcal{W}^{\mathrm{ext}}\left(\boldsymbol{\varphi}; \delta\boldsymbol{\varphi}\right) \qquad \forall \delta\boldsymbol{\varphi} \in \mathcal{V}_{\delta} \tag{25}$$

where $\mathcal{V}$ and $\mathcal{V}_\delta$ are function spaces (with sufficient regularity) to which the placement map and its variation, respectively, belong.

The inertia, internal and external virtual work contributions are given (in the reference configuration) as

$$\mathcal{W}^{\text{ine}} = \int_{\mathcal{B}_0} \rho_0 \delta\boldsymbol{\varphi} \cdot \ddot{\boldsymbol{\varphi}} \, \mathrm{d}\mathcal{B}_0 \tag{26}$$

$$\mathcal{W}^{\text{ext}} = \int_{\mathcal{B}_0} \rho_0 \delta\boldsymbol{\varphi} \cdot \boldsymbol{b} \, \mathrm{d}\mathcal{B}_0 + \int_{\Omega_0} \delta\boldsymbol{\varphi} \cdot \boldsymbol{t}_1 \, \mathrm{d}\Omega_0 \tag{27}$$

$$\mathcal{W}^{\text{int}} = \int_{\mathcal{B}_0} \delta\boldsymbol{F} : \boldsymbol{P} \, \mathrm{d}\mathcal{B}_0 \tag{28}$$

where $\boldsymbol{b}$ is the body force per unit volume, $\boldsymbol{t}_1 = \boldsymbol{P} \cdot \boldsymbol{N}$ is the nominal traction vector on the outer boundary Ω_0 with normal $\boldsymbol{N}$, and $\boldsymbol{P}$ is the first Piola-Kirchhoff stress tensor.

To obtain the explicit form of the internal virtual work we note that this contribution can be reformulated by using Eq. (17), (20) and (23), which yields

$$\mathcal{W}^{\text{int}} = \int_{\mathcal{B}_0} \delta\boldsymbol{g}_i^{\text{b}} \cdot \boldsymbol{P}\boldsymbol{G}^i \, \mathrm{d}\mathcal{B}_0 + \sum_{k=1}^{\text{N}_{\text{del}}} \int_{\Gamma_k} \delta[\![\boldsymbol{\varphi}]\!]_k \cdot \boldsymbol{t}_{\text{coh}} \, \mathrm{d}\Gamma_k \tag{29}$$

where $\boldsymbol{t}_{\text{coh}}$ is the (continuous) degrading normal traction on the delamination surface (with respect to the surface normal $\boldsymbol{N} = \boldsymbol{G}^3$), which in the present approach will be represented by a cohesive zone law as a function of the delamination discontinuity, cf. Section 5. Furthermore, $\delta[\![\boldsymbol{\varphi}]\!]_k$ is the variation of the discontinuity jump at delamination interface number k.

5. Modeling of delamination crack propagation

With the current modeling concept, any cohesive zone model can be adopted to describe the material degradation in the interlaminar region. In the current paper, we employ a (rather standard) bilinear mixed mode cohesive zone model discussed *e.g.* by Fagerström and Larsson [17][3]. Without

[3]It should be remarked that in the current implementation, a minor modification of the model is made with respect to how it is presented in Reference [17] in order to allow for a calibration for pure mode I *and* mode II crack propagation simultaneously. The details of this modification is however out of the scope of the current paper and it is noteworthy

going into details here, it is remarked that the cohesive zone model which we utilize in this paper is formulated in an objective[4] way in terms of material quantities in the finite deformation setting, meaning that the results are consistent also in the case of finite strains and/or rotations. In addition, in its original setting the cohesive zone model also contains a potential rate-dependence which could be of importance in the modeling of certain (thermoplastic) composites with a significant viscous behavior; or in the case of significant delamination propagation associated with fibre bridging. However, since the focus of the current paper is on the kinematical representation of multiple delaminations in shell analyses, only the basic features of the model has an influence on the results. As a consequence, only these features are described and discussed in the current section.

To simplify the discussion and avoid a shift of focus of the paper, we choose to describe the model response for the case of small deformations and rotations. For example, the difference in normal direction of two mutual surfaces of a delamination crack is neglected. If this is the case, the response of the model is as described schematically in Figure 4. In pure mode I, cf. Figure 4a, the model response is elastic in tension (with an elastic stiffness k_n) up to a limiting maximum normal stress value σ_{fn}, after which linear softening is considered in analogy to an elastoplastic damage law. Thus, during unloading the traction decrease proportionally to the decreasing crack opening displacement $[\![\boldsymbol{\varphi}]\!]_n$ related by the damaged elastic stiffness $(1-d)k_n$ with d being an isotropic damage variable. In the reversed loading case (compression where $[\![\boldsymbol{\varphi}]\!]_n < 0$), an additional contact (penalty) stiffness k_c is introduced in such a way that also fully damaged zones transfer compressive loads at only minimal interpenetration between the laminae. As for pure mode II behavior, cf. Figure 4b, the model response is similar to the mode I tension response – but with a maximum shear stress of σ_{fs} – although independent of the actual sign of the crack sliding displacement $[\![\boldsymbol{\varphi}]\!]_s$.

Remark. Naturally, damage also develops for the case of mixed mode loading. However, since the examples considered in the current paper for delamination propagation are idealized for either mode I or mode II crack propagation, the discussion of the mixed mode case is excluded.

---

that the same effect could be accomplished with using the original model with an adjusted input for the mode II fracture energy.

[4]Invariant under a change of observer

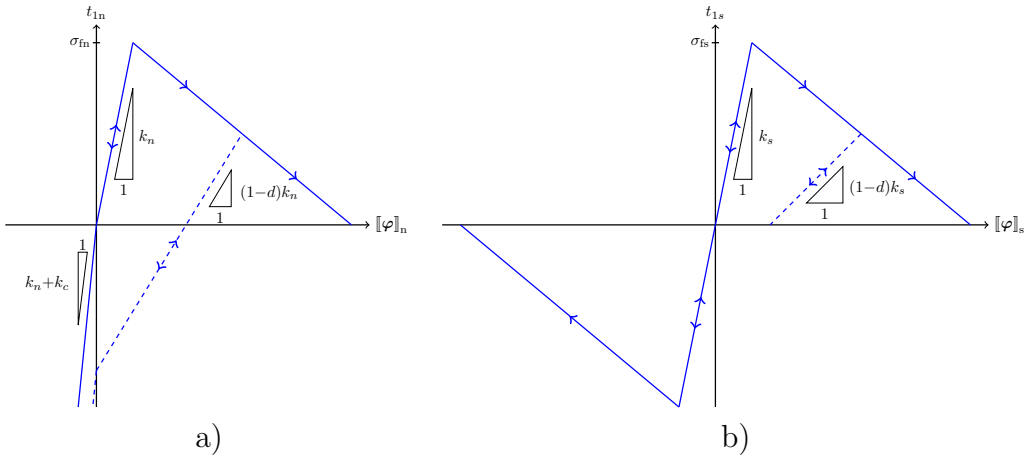

Figure 4: Schematic of a) the pure mode I and b) pure mode II response of the mixed mode cohesive zone model adopted in the current paper.

6. Prototype shell formulation

In this section we exemplify the proposed discontinuity enrichment by selecting a shell formulation and then derive the corresponding shell equations. For this purpose, we adopt the same basic shell formulation as was used by Larsson *et al.* [18] to model through-thickness crack propagation in thinwalled metals. To illustrate our modeling concept and present a self containing (extended) shell formulation, we choose to present all the necessary features of the underlying shell formulation.

As a starting point, the placement map for the reference (undeformed) configuration in Eq. (1) is parameterized as

$$\boldsymbol{\Phi}(\boldsymbol{\xi}) = \bar{\boldsymbol{\Phi}}(\bar{\boldsymbol{\xi}}) + \xi \boldsymbol{M}(\bar{\boldsymbol{\xi}}) \text{ with } \bar{\boldsymbol{\xi}} \in \bar{\Gamma}_0 \text{ and } \xi \in \frac{h_0}{2}[-1,1]. \tag{30}$$

In Eq (30), the mapping $\boldsymbol{\Phi}$ is defined by the mid-surface placement $\bar{\boldsymbol{\Phi}}$ and the outward unit normal director field $\boldsymbol{M}$ defined on the initial mid-surface $\bar{\Gamma}_0$ (with $|\boldsymbol{M}| = 1$) and with h_0 being the initial thickness of the shell. The corresponding co-variant base vectors in the initial configuration thereby become

$$\begin{cases} \boldsymbol{G}_\alpha = \bar{\boldsymbol{\Phi}}_{,\alpha} + \xi \boldsymbol{M}_{,\alpha} \\ \boldsymbol{G}_3 = \boldsymbol{M} \end{cases} \tag{31}$$

where the base vectors associated with the tangent plane are indicated with subindex $\alpha = 1, 2$ and where $\boldsymbol{G}^3 = \boldsymbol{G}_3 = \boldsymbol{M}$.

6.1. Continuous part of the deformation map

For the continuous part of the deformation map $\boldsymbol{\varphi}^{\mathrm{c}}$ in Eq. (10) the following parametrization of the shell geometry is used

$$\boldsymbol{\varphi}^{\mathrm{c}}(\boldsymbol{\xi}) = \bar{\boldsymbol{\varphi}}^{\mathrm{c}}(\bar{\boldsymbol{\xi}}) + \xi \boldsymbol{m}^{\mathrm{c}}(\bar{\boldsymbol{\xi}}) + \frac{1}{2}\xi^2 \gamma^{\mathrm{c}}(\bar{\boldsymbol{\xi}}) \boldsymbol{m}(\bar{\boldsymbol{\xi}}) \tag{32}$$

where the deformed geometry is described in terms of the current mid-surface placement $\bar{\boldsymbol{\varphi}}^{\mathrm{c}}$, the extensible director field $\boldsymbol{m}^{\mathrm{c}}$ and an additional scalar thickness strain γ^{c} (leading to seven degrees of freedom). Thus, the current shell formulation have three unknown fields describing the continuous deformation which we collect in the column array $\hat{\boldsymbol{p}}^{\mathrm{c}}$ as

$$\hat{\boldsymbol{p}}^{\mathrm{c}} = \begin{pmatrix} \bar{\boldsymbol{\varphi}}^{\mathrm{c}} & \boldsymbol{m}^{\mathrm{c}} & \gamma^{\mathrm{c}} \end{pmatrix}^{\mathrm{T}} \tag{33}$$

The corresponding co-variant base vectors in the deformed configuration, defined in Eq. (18), are obtained as follows

$$\begin{cases} \boldsymbol{g}^c_\alpha &= \bar{\boldsymbol{\varphi}}_{,\alpha} + \left(\xi + \frac{1}{2}\gamma\xi^2\right) \boldsymbol{m}_{,\alpha} + \frac{1}{2}\gamma_{,\alpha}\xi^2 \boldsymbol{m}, \ \alpha = 1, 2 \\ \boldsymbol{g}^c_3 &= (1 + \gamma\xi)\, \boldsymbol{m} \end{cases} \tag{34}$$

From Eq. (32) it is seen that the deformation map corresponds to a second order Taylor expansion along the director field involving the strain γ^{c}. This higher order expansion allows for an inhomogeneous thickness strain and is introduced in order to avoid the pathological volumetric locking observed for shells with constant thickness strains, see *e.g.* [19].

6.2. Discontinuous part of the deformation map

To (kinematically) represent delaminations in the current shell formulation, both the mid-surface placement and director must be discontinuous over the delamination interface. Thus, for each enrichment a discontinuous mid-surface placement $\bar{\boldsymbol{\varphi}}^{\mathrm{d}}_k$ and director $\boldsymbol{m}^{\mathrm{d}}_k$ are introduced, cf. [16], such that Eq. (11) can be written as

$$\boldsymbol{\varphi}^{\mathrm{d}} = \sum_{k=1}^{\mathrm{N_{del}}} \psi_k \, \left(\bar{\boldsymbol{\varphi}}^{\mathrm{d}}_k(\bar{\boldsymbol{\xi}}) + \xi \boldsymbol{m}^{\mathrm{d}}_k(\bar{\boldsymbol{\xi}})\right). \tag{35}$$

We here choose not to enrich the γ-field since its contribution to the deformation is usually negligible and, as mentioned in the previous section, its

main purpose is to alleviate locking. Furthermore, it also results in a more computationally efficient formulation. The co-variant base vectors associated with the discontinuous deformation maps $\boldsymbol{\varphi}_k^{\mathrm{d}}$ takes the following short form

$$\begin{cases} \boldsymbol{g}_{k\alpha}^{\mathrm{d}} = \bar{\boldsymbol{\varphi}}_{k,\alpha}^{\mathrm{d}} + \xi \boldsymbol{m}_{k,\alpha}^{\mathrm{d}} & \alpha = 1,2 \\ \boldsymbol{g}_{k3}^{\mathrm{d}} = \boldsymbol{m}^{\mathrm{d}_k} \end{cases} \tag{36}$$

Similarly to the continuous deformation map, the involved unknown fields at a given mid-surface coordinate $\bar{\boldsymbol{\xi}}$, associated with discontinuity number k, are collected into the column vector

$$\hat{\boldsymbol{p}}_k^{\mathrm{d}} = \begin{pmatrix} \bar{\boldsymbol{\varphi}}_k^{\mathrm{d}} & \boldsymbol{m}_k^{\mathrm{d}} \end{pmatrix}^{\mathrm{T}} \tag{37}$$

and an array containing all the unknown fields is defined as

$$\hat{\boldsymbol{p}} = \begin{pmatrix} \hat{\boldsymbol{p}}^{\mathrm{c}} \\ \{\hat{\boldsymbol{p}}_k^{\mathrm{d}}\} \end{pmatrix} \tag{38}$$

Here, we have introduced the compact notation of using $\{\bullet\}$ to indicate all the solution arrays, $(k = 1, \ldots, \mathrm{N_{del}})$. Thus, the equation above is shorthand for

$$\hat{\boldsymbol{p}} = \begin{pmatrix} \hat{\boldsymbol{p}}^{\mathrm{c}} \\ \hat{\boldsymbol{p}}_1^{\mathrm{d}} \\ \vdots \\ \hat{\boldsymbol{p}}_{\mathrm{N_{del}}}^{\mathrm{d}} \end{pmatrix}. \tag{39}$$

This array notation is used throughout the rest of the paper and the exact meaning is given by the context.

Finally, the deformation gradient can be expressed for this particular shell formulation by inserting Eqs. (6), (31) and (36) into Eq. (15)-(20). From the deformation gradient, the stresses can be computed in any point in the shell.

6.3. Variation of placement maps

First, we note that the variation of the placement map in Eq. (10) is obtained as

$$\delta\boldsymbol{\varphi} = \delta\boldsymbol{\varphi}^{\mathrm{c}} + \delta\boldsymbol{\varphi}^{\mathrm{d}}, \tag{40}$$

which can be expressed in a matrix form as

$$\delta\boldsymbol{\varphi} = \boldsymbol{\Upsilon}^{\mathrm{c}}(\hat{\boldsymbol{p}}^{\mathrm{c}})\delta\hat{\boldsymbol{p}}^{\mathrm{c}} + \psi_k \boldsymbol{\Upsilon}_k^{\mathrm{d}} \delta\hat{\boldsymbol{p}}_k^{\mathrm{d}} = \boldsymbol{\Upsilon}\delta\hat{\boldsymbol{p}} \tag{41}$$

with the matrices

$$\boldsymbol{\Upsilon}^{\mathrm{c}} = \begin{pmatrix} \mathbf{I} & a\mathbf{I} & b\boldsymbol{m}^{\mathrm{c}} \end{pmatrix} \tag{42}$$

$$\boldsymbol{\Upsilon}^{\mathrm{d}}_k = \begin{pmatrix} \mathbf{I} & \xi\mathbf{I} \end{pmatrix} \tag{43}$$

$$\boldsymbol{\Upsilon} = \begin{pmatrix} \boldsymbol{\Upsilon}^{\mathrm{c}} & \left\{\psi_k \boldsymbol{\Upsilon}^{\mathrm{d}}_k\right\} \end{pmatrix} \tag{44}$$

and variations of the solution vectors in Eq. (33), (37) and (38)

$$\delta\hat{\boldsymbol{p}}^{\mathrm{c}} = \begin{pmatrix} \delta\bar{\boldsymbol{\varphi}}^{\mathrm{c}} & \delta\boldsymbol{m}^{\mathrm{c}} & \delta\gamma^{\mathrm{c}} \end{pmatrix}^{\mathrm{T}} \tag{45}$$

$$\delta\hat{\boldsymbol{p}}^{\mathrm{d}}_k = \begin{pmatrix} \delta\bar{\boldsymbol{\varphi}}^{\mathrm{d}}_k & \delta\boldsymbol{m}^{\mathrm{d}}_k \end{pmatrix}^{\mathrm{T}} \tag{46}$$

$$\delta\hat{\boldsymbol{p}} = \begin{pmatrix} \delta\hat{\boldsymbol{p}}^{\mathrm{c}} \\ \left\{\delta\hat{\boldsymbol{p}}^{\mathrm{d}}_k\right\} \end{pmatrix} \tag{47}$$

where we also introduced the coefficients

$$\begin{cases} a = \xi + \frac{1}{2}\xi^2\gamma, \\ b = \frac{1}{2}\xi^2. \end{cases} \tag{48}$$

6.4. Variation of base vectors

Similarly to the deformation map, the variation of the base vectors associated with the continuous deformation map in Eq. (34) can be expressed as

$$\delta\boldsymbol{g}^{\mathrm{c}}_i(\boldsymbol{\xi}) = \boldsymbol{\Lambda}^{\mathrm{c}}_i(\hat{\boldsymbol{p}}^{\mathrm{c}})\delta\hat{\boldsymbol{n}}^{\mathrm{c}} \tag{49}$$

where $\delta\hat{\boldsymbol{n}}^{\mathrm{c}}$ is the variation of an array $\hat{\boldsymbol{n}}^{\mathrm{c}}$ containing deformation measure fields (associated with the continuous deformation map) defined as

$$\hat{\boldsymbol{n}}^{\mathrm{c}} = \begin{pmatrix} \bar{\boldsymbol{\varphi}}^{\mathrm{c}}_{,1} & \bar{\boldsymbol{\varphi}}^{\mathrm{c}}_{,2} & \boldsymbol{m}^{\mathrm{c}}_{,1} & \boldsymbol{m}^{\mathrm{c}}_{,2} & \boldsymbol{m}^{\mathrm{c}} & \gamma^{\mathrm{c}}_{,1} & \gamma^{\mathrm{c}}_{,2} & \gamma^{\mathrm{c}} \end{pmatrix}^{\mathrm{T}} \tag{50}$$

This array can be seen as a generalized strain measure containing: mid-surface stretches $(\bar{\boldsymbol{\varphi}}^{\mathrm{c}}_{,1}, \bar{\boldsymbol{\varphi}}^{\mathrm{c}}_{,2})$, curvature like quantities $(\boldsymbol{m}^{\mathrm{c}}_{,1}, \boldsymbol{m}^{\mathrm{c}}_{,2})$ and thickness associated stretch quantities $(\boldsymbol{m}^{\mathrm{c}}, \gamma^{\mathrm{c}}_{,1}, \gamma^{\mathrm{c}}_{,2}, \gamma^{\mathrm{c}})$. The variation is obtained as

$$\delta\hat{\boldsymbol{n}}^{\mathrm{c}} = \begin{pmatrix} \delta\bar{\boldsymbol{\varphi}}^{\mathrm{c}}_{,1} & \delta\bar{\boldsymbol{\varphi}}^{\mathrm{c}}_{,2} & \delta\boldsymbol{m}^{\mathrm{c}}_{,1} & \delta\boldsymbol{m}^{\mathrm{c}}_{,2} & \delta\boldsymbol{m}^{\mathrm{c}} & \delta\gamma^{\mathrm{c}}_{,1} & \delta\gamma^{\mathrm{c}}_{,2} & \delta\gamma^{\mathrm{c}} \end{pmatrix}^{\mathrm{T}} \tag{51}$$

where $\boldsymbol{\Lambda}_i$ above are the matrices (of size 3×18)

$$\boldsymbol{\Lambda}^{\mathrm{c}}_1 = \begin{pmatrix} \mathbf{I} & \mathbf{0} & a\mathbf{I} & \mathbf{0} & b\gamma_{,1}\mathbf{I} & b\boldsymbol{m} & \mathbf{0} & b\boldsymbol{m}_{,1} \end{pmatrix} \tag{52}$$

$$\boldsymbol{\Lambda}^{\mathrm{c}}_2 = \begin{pmatrix} \mathbf{0} & \mathbf{I} & \mathbf{0} & a\mathbf{I} & b\gamma_{,2}\mathbf{I} & \mathbf{0} & b\boldsymbol{m} & b\boldsymbol{m}_{,2} \end{pmatrix} \tag{53}$$

$$\boldsymbol{\Lambda}^{\mathrm{c}}_3 = \begin{pmatrix} \mathbf{0} & \mathbf{0} & \mathbf{0} & \mathbf{0} & c\mathbf{I} & \mathbf{0} & \mathbf{0} & \xi\boldsymbol{m} \end{pmatrix} \tag{54}$$

where we also introduced the additional coefficient

$$c = 1 + \xi\gamma. \tag{55}$$

In analogy with Eq. (49), the variation of the base vectors associated with discontinuous placement maps, cf. Eq. (36), can be expressed as

$$\delta \boldsymbol{g}^{\mathrm{d}}_{ki}(\boldsymbol{\xi}) = \psi_k \boldsymbol{\Lambda}^{\mathrm{d}}_{ki} \delta \hat{\boldsymbol{n}}^{\mathrm{d}}_k \tag{56}$$

where $\delta\hat{\boldsymbol{n}}^{\mathrm{d}}_k$ is the variation of the deformation measure array $\hat{\boldsymbol{n}}^{\mathrm{d}}_k$ (one for each delamination) defined as

$$\hat{\boldsymbol{n}}^{\mathrm{d}}_k = \begin{pmatrix} \bar{\boldsymbol{\varphi}}^{\mathrm{d}}_{k,1} & \bar{\boldsymbol{\varphi}}^{\mathrm{d}}_{k,2} & \boldsymbol{m}^{\mathrm{d}}_{k,1} & \boldsymbol{m}^{\mathrm{d}}_{k,2} & \boldsymbol{m}^{\mathrm{d}}_{k} \end{pmatrix}^{\mathrm{T}} \tag{57}$$

such that

$$\delta\hat{\boldsymbol{n}}^{\mathrm{d}}_k = \begin{pmatrix} \delta\bar{\boldsymbol{\varphi}}^{\mathrm{d}}_{k,1} & \delta\bar{\boldsymbol{\varphi}}^{\mathrm{d}}_{k,2} & \delta\boldsymbol{m}^{\mathrm{d}}_{k,1} & \delta\boldsymbol{m}^{\mathrm{d}}_{k,2} & \delta\boldsymbol{m}^{\mathrm{d}}_{k} \end{pmatrix}^{\mathrm{T}} \tag{58}$$

and where $\boldsymbol{\Lambda}^{\mathrm{d}}_{ki}$ are the matrices (of size 3×15)

$$\boldsymbol{\Lambda}^{\mathrm{d}}_{k1} = \begin{pmatrix} \mathbf{I} & \mathbf{0} & \xi\mathbf{I} & \mathbf{0} & \mathbf{0} \end{pmatrix} \tag{59}$$

$$\boldsymbol{\Lambda}^{\mathrm{d}}_{k2} = \begin{pmatrix} \mathbf{0} & \mathbf{I} & \mathbf{0} & \xi\mathbf{I} & \mathbf{0} \end{pmatrix} \tag{60}$$

$$\boldsymbol{\Lambda}^{\mathrm{d}}_{k3} = \begin{pmatrix} \mathbf{0} & \mathbf{0} & \mathbf{0} & \mathbf{0} & \mathbf{I} \end{pmatrix} \tag{61}$$

Note that $\boldsymbol{\Lambda}^{\mathrm{d}}_{ki}$ are identical for all delamination enrichments and are not dependent on the solution fields (in contrast to $\boldsymbol{\Lambda}^{\mathrm{c}}_i$).

Finally the variation of the base vectors $\boldsymbol{g}^{\mathrm{b}}_i$, in Eq. (17), can be written with the help of Eqs. (49) and (56) as

$$\delta \boldsymbol{g}^{\mathrm{b}}_i = \delta \boldsymbol{g}^{\mathrm{c}}_i + \sum_{k=1}^{\mathrm{N_{del}}} \delta \boldsymbol{g}^{\mathrm{d}}_{ki} = \boldsymbol{\Lambda}^{\mathrm{c}}_i \delta \hat{\boldsymbol{n}}^{\mathrm{c}} + \sum_{k=1}^{\mathrm{N_{del}}} \psi_k \boldsymbol{\Lambda}^{\mathrm{d}}_{ki} \delta \hat{\boldsymbol{n}}^{\mathrm{d}}_k = \boldsymbol{\Lambda}_i \cdot \delta\hat{\boldsymbol{n}} \tag{62}$$

with

$$\boldsymbol{\Lambda}_i = \begin{pmatrix} \boldsymbol{\Lambda}^{\mathrm{c}}_i & \left\{ \psi_k \boldsymbol{\Lambda}^{\mathrm{d}}_{ki} \right\} \end{pmatrix} \tag{63}$$

and

$$\delta\hat{\boldsymbol{n}} = \begin{pmatrix} \delta\hat{\boldsymbol{n}}^{\mathrm{c}} \\ \left\{ \delta\hat{\boldsymbol{n}}^{\mathrm{d}}_k \right\} \end{pmatrix}. \tag{64}$$

In the next section, the weak form will be derived for the proposed shell kinematics making use of Eqs. (41) and (62).

7. Momentum balance in terms of shell kinematics

To further illustrate the proposed XFEM enrichment, the momentum balance needs to be expressed in terms of the assumed shell kinematics. We start with the inertial work where it is seen that the adopted shell kinematics results in a non-standard term. Then the external and internal work is presented and it is shown how the internal work can be interpreted as sectional forces.

7.1. Inertial work

By noting that the time derivative of the placement map follows the same structure as the variation, we directly obtain from Eq. (41)

$$\dot{\boldsymbol{\varphi}} = \boldsymbol{\Upsilon}^{\mathrm{c}}\dot{\hat{\boldsymbol{p}}}^{\mathrm{c}} + \boldsymbol{\Upsilon}^{\mathrm{d}}\dot{\hat{\boldsymbol{p}}}^{\mathrm{d}}_{k} = \boldsymbol{\Upsilon}\dot{\hat{\boldsymbol{p}}} \tag{65}$$

$$\ddot{\boldsymbol{\varphi}} = \boldsymbol{\Upsilon}^{\mathrm{c}}\ddot{\hat{\boldsymbol{p}}}^{\mathrm{c}} + \dot{\boldsymbol{\Upsilon}}^{\mathrm{c}}\dot{\hat{\boldsymbol{p}}}^{\mathrm{c}} + \boldsymbol{\Upsilon}^{\mathrm{d}}\ddot{\hat{\boldsymbol{p}}}^{\mathrm{d}}_{k} = \boldsymbol{\Upsilon}\ddot{\hat{\boldsymbol{p}}} + \dot{\boldsymbol{\Upsilon}}\dot{\hat{\boldsymbol{p}}} \tag{66}$$

which together with Eq. (26) and Eq. (41) again gives

$$\begin{aligned}\mathcal{W}^{\mathrm{ine}} &= \int_{\mathcal{B}_0} \rho_0 \delta\boldsymbol{\varphi} \cdot \ddot{\boldsymbol{\varphi}}\, \mathrm{d}\mathcal{B}_0 = \int_{\mathcal{B}_0} \rho_0 \boldsymbol{\Upsilon}\delta\hat{\boldsymbol{p}} \cdot \left(\boldsymbol{\Upsilon}\ddot{\hat{\boldsymbol{p}}} + \dot{\boldsymbol{\Upsilon}}\dot{\hat{\boldsymbol{p}}}\right) \mathrm{d}\mathcal{B}_0 \\ &= \int_{\mathcal{B}_0} \rho_0 \delta\hat{\boldsymbol{p}}^{\mathrm{T}} \left(\boldsymbol{\Upsilon}^{\mathrm{T}}\boldsymbol{\Upsilon}\right) \ddot{\hat{\boldsymbol{p}}}\, \mathrm{d}\mathcal{B}_0 + \int_{\mathcal{B}_0} \rho_0 \delta\hat{\boldsymbol{p}}^{\mathrm{T}} \left(\boldsymbol{\Upsilon}^{\mathrm{T}}\dot{\boldsymbol{\Upsilon}}\right) \dot{\hat{\boldsymbol{p}}}\, \mathrm{d}\mathcal{B}_0 \end{aligned} \tag{67}$$

Note that the non-standard term in Eq. $(67)_2$ corresponds to a (convective) force term which appears due to the second order expansion in the thickness direction, cf. Eq. (32). It involves contributions from the first order time derivatives of unknown fields $\hat{\boldsymbol{p}}$ as described in Reference [18].

7.2. External work

We consider a shell subjected to body forces $\boldsymbol{b}_0$ and a prescribed traction $\boldsymbol{t}_1$ such that the external work can be written as

$$\mathcal{W}^{\mathrm{ext}} = \int_{\mathcal{B}_0} \rho_0 \delta\hat{\boldsymbol{p}}^{\mathrm{T}}\boldsymbol{\Upsilon}^{\mathrm{T}} \cdot \boldsymbol{b}\, \mathrm{d}\mathcal{B}_0 + \int_{\Omega_0} \delta\hat{\boldsymbol{p}}^{\mathrm{T}}\boldsymbol{\Upsilon}^{\mathrm{T}} \cdot \boldsymbol{t}_1\, \mathrm{d}\Omega_0 \tag{68}$$

7.3. Internal work

With Eqs. (29) and (62), we note that the internal work can be written as

$$\mathcal{W}^{\text{int}} = \int_{\mathcal{B}_0} \delta\hat{\boldsymbol{n}}^{\text{T}} \cdot \boldsymbol{\Lambda}_i^{\text{T}} \boldsymbol{P}\boldsymbol{G}^i \, \text{d}\mathcal{B}_0 + \sum_{k=1}^{\text{N}_{\text{del}}} \int_{\Gamma_k} \delta[\![\boldsymbol{\varphi}]\!]_k \cdot \boldsymbol{t}_{\text{coh}} \, \text{d}\Gamma_k \tag{69}$$

Remark. Sectional forces or stress resultants, commonly used in shell formulations, may be defined by subdividing the volume integral in Eq. $(69)_1$ into an in-plane integration over the initial mid-surface $\bar{\Gamma}_0$ and a thickness integration over h_0. This can be achieved, cf. [18], by recognizing that $\hat{\boldsymbol{n}}$ is defined on the mid-surface and thus independent of ξ. We obtain for the differential volume element

$$\text{d}\mathcal{B}_0 = \, \text{d}\bar{\Gamma}_0 \, \text{d}h \tag{70}$$

which gives

$$\int_{\mathcal{B}_0} \delta\hat{\boldsymbol{n}}^{\text{T}} \boldsymbol{\Lambda}_i^{\text{T}} \boldsymbol{P}\boldsymbol{G}^i \, \text{d}\mathcal{B}_0 = \int_{\bar{\Gamma}_0} \delta\hat{\boldsymbol{n}}^{\text{T}} \hat{\boldsymbol{N}} \, \text{d}\bar{\Gamma}_0 \tag{71}$$

with the sectional forces $\hat{\boldsymbol{N}}$ defined as

$$\hat{\boldsymbol{N}} = \int_{-h_0/2}^{h_0/2} \boldsymbol{\Lambda}_i^{\text{T}} \boldsymbol{P}\boldsymbol{G}^i \, \text{d}h \tag{72}$$

7.4. Weak from of momentum balance

Combining Eqs.(67)-(69), the final weak form, cf. Eq. (25), can with respect to the current prototype shell element formulation be written as

$$\begin{aligned} &\int_{\mathcal{B}_0} \rho_0 \delta\hat{\boldsymbol{p}}^{\text{T}} \left(\boldsymbol{\Upsilon}^{\text{T}} \boldsymbol{\Upsilon}\right) \ddot{\hat{\boldsymbol{p}}} \, \text{d}\mathcal{B}_0 + \int_{\mathcal{B}_0} \rho_0 \delta\hat{\boldsymbol{p}}^{\text{T}} \left(\boldsymbol{\Upsilon}^{\text{T}} \dot{\boldsymbol{\Upsilon}}\right) \dot{\hat{\boldsymbol{p}}} \, \text{d}\mathcal{B}_0 \\ &+ \int_{\mathcal{B}_0} \delta\hat{\boldsymbol{n}}^{\text{T}} \cdot \boldsymbol{\Lambda}_i^{\text{T}} \boldsymbol{P}\boldsymbol{G}^i \, \text{d}\mathcal{B}_0 + \sum_{k=1}^{\text{N}_{\text{del}}} \int_{\Gamma_k} \delta[\![\boldsymbol{\varphi}]\!]_k \cdot \boldsymbol{t}_{\text{coh}} \, \text{d}\Gamma_k \\ &= \int_{\mathcal{B}_0} \rho_0 \delta\hat{\boldsymbol{p}}^{\text{T}} \boldsymbol{\Upsilon}^{\text{T}} \cdot \boldsymbol{b} \, \text{d}\mathcal{B}_0 + \int_{\Omega_0} \delta\hat{\boldsymbol{p}}^{\text{T}} \boldsymbol{\Upsilon}^{\text{T}} \cdot \boldsymbol{t}_1 \, \text{d}\Omega_0. \end{aligned} \tag{73}$$

8. FE approximations

In this section, the pertaining FE equations of the weak form is established on an elemental basis to keep the notation simple. The shell formulation contains one set of continuous solution fields, $\hat{\boldsymbol{p}}^{\mathrm{c}}$ and several discontinuous ones, $\{\hat{\boldsymbol{p}}_k^{\mathrm{d}}\}$, as described in Section 6. Each of these fields are approximated over the element, in a standard manner, using finite element shape functions, as

$$\bar{\boldsymbol{\varphi}}^{\mathrm{c}} \approx \boldsymbol{N}_{\varphi}\hat{\bar{\boldsymbol{\varphi}}}^{\mathrm{c}} \qquad \boldsymbol{m}^{\mathrm{c}} \approx \boldsymbol{N}_{m}\hat{\boldsymbol{m}}^{\mathrm{c}} \qquad \gamma \approx \boldsymbol{N}_{\gamma}\hat{\boldsymbol{\gamma}} \tag{74}$$

for the continuous fields and likewise for the discontinuous fields

$$\bar{\boldsymbol{\varphi}}_k^{\mathrm{d}} \approx \boldsymbol{N}_{\varphi}\hat{\bar{\boldsymbol{\varphi}}}_k^{\mathrm{d}} \qquad \boldsymbol{m}_k^{\mathrm{d}} \approx \boldsymbol{N}_{m}\hat{\boldsymbol{m}}_k^{\mathrm{d}}. \tag{75}$$

Here, $\boldsymbol{N}_{\varphi}$, $\boldsymbol{N}_{m}$ and $\boldsymbol{N}_{\gamma}$ are the shape function matrices associated with the interpolation of the mid-surface placement, director field and gamma field, respectively (both continuous and discontinuous). The arrays $\hat{\bar{\boldsymbol{\varphi}}}^{\mathrm{c}}$, $\hat{\boldsymbol{m}}^{\mathrm{c}}$, $\hat{\boldsymbol{\gamma}}$, $\hat{\boldsymbol{\varphi}}_k^{\mathrm{d}}$ and $\hat{\boldsymbol{m}}_k^{\mathrm{d}}$ are the (unknown) element solution vectors. Furthermore, as seen from Eq. (75) above, an isoparametric approximation is used for the continuous and discontinuous fields. This also holds for the initial geometry such that

$$\bar{\boldsymbol{\Phi}} \approx \boldsymbol{N}_{\varphi}\hat{\bar{\boldsymbol{\Phi}}} \qquad \boldsymbol{M} \approx \boldsymbol{N}_{m}\hat{\boldsymbol{M}}. \tag{76}$$

By combining Eqs. (33), (37), (74) and (75), the array of solution fields $\hat{\boldsymbol{p}}$ can be written as

$$\hat{\boldsymbol{p}} = \begin{pmatrix} \hat{\boldsymbol{p}}^{\mathrm{c}} \\ \hat{\boldsymbol{p}}_k^{\mathrm{d}} \end{pmatrix} \approx \begin{pmatrix} \boldsymbol{N}^{\mathrm{c}} & \boldsymbol{0} \\ \boldsymbol{0} & \{\boldsymbol{N}_k^{\mathrm{d}}\} \end{pmatrix} \begin{pmatrix} \boldsymbol{a}^{\mathrm{c}} \\ \{\boldsymbol{a}_k^{\mathrm{d}}\} \end{pmatrix} = \boldsymbol{N}\boldsymbol{a} \tag{77}$$

where the N-matrices associated with the continuous and discontinuous part of the solution fields have been introduced as

$$\boldsymbol{N}^{\mathrm{c}} = \begin{pmatrix} \boldsymbol{N}_{\varphi} & \boldsymbol{0} & \boldsymbol{0} \\ \boldsymbol{0} & \boldsymbol{N}_{m} & \boldsymbol{0} \\ \boldsymbol{0} & \boldsymbol{0} & \boldsymbol{N}_{\gamma} \end{pmatrix} \qquad \boldsymbol{N}_k^{\mathrm{d}} = \begin{pmatrix} \boldsymbol{N}_{\varphi} & \boldsymbol{0} \\ \boldsymbol{0} & \boldsymbol{N}_{m} \end{pmatrix} \tag{78}$$

and where we have the continuous and discontinuous solution vectors

$$\boldsymbol{a}^{\mathrm{c}} = \begin{pmatrix} \hat{\boldsymbol{\varphi}}^{\mathrm{c}} \\ \hat{\boldsymbol{m}}^{\mathrm{c}} \\ \hat{\boldsymbol{\gamma}} \end{pmatrix} \qquad \boldsymbol{a}_k^{\mathrm{d}} = \begin{pmatrix} \hat{\boldsymbol{\varphi}}_k^{\mathrm{d}} \\ \hat{\boldsymbol{m}}_k^{\mathrm{d}} \end{pmatrix}. \tag{79}$$

It follows directly from Eq. (77) that the time derivatives of the solution fields can be expressed as

$$\dot{\hat{\boldsymbol{p}}} = \boldsymbol{N}\dot{\boldsymbol{a}} \qquad \text{and} \qquad \ddot{\hat{\boldsymbol{p}}} = \boldsymbol{N}\ddot{\boldsymbol{a}}. \tag{80}$$

From the chosen approximations of the solution fields, the deformation array $\hat{\boldsymbol{n}}$ can be written in a similar manner to Eq. (77) as

$$\hat{\boldsymbol{n}} = \begin{pmatrix} \hat{\boldsymbol{n}}^{\mathrm{c}} \\ \hat{\boldsymbol{n}}^{\mathrm{d}}_k \end{pmatrix} \approx \begin{pmatrix} \boldsymbol{B}^{\mathrm{c}} & \boldsymbol{0} \\ \boldsymbol{0} & \{\boldsymbol{B}^{\mathrm{d}}_k\} \end{pmatrix} \begin{pmatrix} \boldsymbol{a}^{\mathrm{c}} \\ \{\boldsymbol{a}^{\mathrm{d}}_k\} \end{pmatrix} = \boldsymbol{B}\boldsymbol{a} \tag{81}$$

where the introduced matrix $\boldsymbol{B}$ is constructed from the submatrices

$$\boldsymbol{B}^{\mathrm{c}} = \begin{pmatrix} \boldsymbol{N}_{\varphi,1} & \boldsymbol{0} & \boldsymbol{0} \\ \boldsymbol{N}_{\varphi,2} & \boldsymbol{0} & \boldsymbol{0} \\ \boldsymbol{0} & \boldsymbol{N}_{m,1} & \boldsymbol{0} \\ \boldsymbol{0} & \boldsymbol{N}_{m,2} & \boldsymbol{0} \\ \boldsymbol{0} & \boldsymbol{N}_{m} & \boldsymbol{0} \\ \boldsymbol{0} & \boldsymbol{0} & \boldsymbol{N}_{\gamma,1} \\ \boldsymbol{0} & \boldsymbol{0} & \boldsymbol{N}_{\gamma,2} \\ \boldsymbol{0} & \boldsymbol{0} & \boldsymbol{N}_{\gamma} \end{pmatrix} \qquad \text{and} \qquad \boldsymbol{B}^{\mathrm{d}}_k = \begin{pmatrix} \boldsymbol{N}_{\varphi,1} & \boldsymbol{0} \\ \boldsymbol{N}_{\varphi,2} & \boldsymbol{0} \\ \boldsymbol{0} & \boldsymbol{N}_{m,1} \\ \boldsymbol{0} & \boldsymbol{N}_{m,2} \\ \boldsymbol{0} & \boldsymbol{N}_{m} \end{pmatrix}. \tag{82}$$

Note that, the array notation in *e.g.* $\boldsymbol{N}$, in Eq. (77), corresponds to several diagonal block matrices as

$$\boldsymbol{N} = \begin{pmatrix} \boldsymbol{N}^{\mathrm{c}} & \boldsymbol{0} & \dots & \boldsymbol{0} \\ \boldsymbol{0} & \boldsymbol{N}^{\mathrm{d}}_1 & \dots & \boldsymbol{0} \\ \vdots & \boldsymbol{0} & \ddots & \boldsymbol{0} \\ \boldsymbol{0} & \dots & \boldsymbol{0} & \boldsymbol{N}^{\mathrm{d}}_{\mathrm{N_{del}}} \end{pmatrix} \tag{83}$$

and similarly for $\boldsymbol{B}$.

8.1. Inertial, internal and external force vectors

In a Galerkin fashion, the variations $\delta\hat{\boldsymbol{p}}$, $\delta\dot{\hat{\boldsymbol{p}}}$ and $\delta\hat{\boldsymbol{n}}$ are approximated in the same way as $\hat{\boldsymbol{p}}$, $\dot{\hat{\boldsymbol{p}}}$ and $\hat{\boldsymbol{n}}$ respectively, such that we obtain

$$\delta\hat{\boldsymbol{p}} = \boldsymbol{N}\delta\boldsymbol{a}, \qquad \delta\dot{\hat{\boldsymbol{p}}} = \boldsymbol{N}\delta\dot{\boldsymbol{a}} \qquad \text{and} \qquad \delta\hat{\boldsymbol{n}} = \boldsymbol{B}\delta\boldsymbol{a}. \tag{84}$$

For the approximation of the discontinuity jump $[\![\boldsymbol{\varphi}]\!]_k$, we note that it is computed from the already approximated solution fields $\hat{\boldsymbol{p}}$ and the variation of the jump $\delta[\![\boldsymbol{\varphi}]\!]_k$ is written as

$$\delta[\![\boldsymbol{\varphi}]\!]_k = \boldsymbol{N}_{k,\mathrm{coh}}\delta\boldsymbol{a} \tag{85}$$

where $\boldsymbol{N}_{k,\mathrm{coh}}$ is constructed from the matrix $\boldsymbol{N}$ evaluated above and below the delamination interface number k.

Introducing the FE-approximations in Eqs. (77), (81), (84) and (85) into the weak form in Eq. (25) leads to the FE equations for the shell element

$$\boldsymbol{M}\ddot{\boldsymbol{a}} + \boldsymbol{M}_{\mathrm{con}}\dot{\boldsymbol{a}} + \boldsymbol{f}_{\mathrm{int}}(\boldsymbol{a}) = \boldsymbol{f}_{\mathrm{ext}} \tag{86}$$

where $\boldsymbol{M}$ is the consistent mass matrix, $\boldsymbol{M}_{\mathrm{con}}$ is a convective mass matrix, $\boldsymbol{f}_{\mathrm{int}}$ is the internal force vector and $\boldsymbol{f}_{\mathrm{ext}}$ is the external force vector. They are all defined as follows

$$\boldsymbol{M} = \int_{\mathcal{B}_0} \rho_0 \boldsymbol{N}^{\mathrm{T}} \boldsymbol{\Upsilon}^{\mathrm{T}} \boldsymbol{\Upsilon} \boldsymbol{N} \, \mathrm{d}\mathcal{B}_0 \tag{87}$$

$$\boldsymbol{M}_{\mathrm{con}} = \int_{\mathcal{B}_0} \rho_0 \delta \boldsymbol{N}^{\mathrm{T}} \boldsymbol{\Upsilon}^{\mathrm{T}} \dot{\boldsymbol{\Upsilon}} \boldsymbol{N} \, \mathrm{d}\mathcal{B}_0 \tag{88}$$

$$\boldsymbol{f}_{\mathrm{int}} = \int_{\mathcal{B}_0} \boldsymbol{B}^{\mathrm{T}} \boldsymbol{\Lambda}_i^{\mathrm{T}} \boldsymbol{P} \boldsymbol{G}^i \, \mathrm{d}\mathcal{B}_0 + \sum_{k=1}^{\mathrm{N_{del}}} \int_{\Gamma_k} \boldsymbol{N}_{k,\mathrm{coh}}^{\mathrm{T}} \boldsymbol{t}_{\mathrm{coh}} \, \mathrm{d}\Gamma_k \tag{89}$$

$$\boldsymbol{f}_{\mathrm{ext}} = \int_{\mathcal{B}_0} \rho_0 \boldsymbol{N}^{\mathrm{T}} \boldsymbol{\Upsilon}^{\mathrm{T}} \boldsymbol{b} \, \mathrm{d}\mathcal{B}_0 + \int_{\Omega_0} \boldsymbol{N}^{\mathrm{T}} \boldsymbol{\Upsilon}^{\mathrm{T}} \tilde{\boldsymbol{t}}_1 \, \mathrm{d}\Omega_0. \tag{90}$$

9. Numerical examples for validation of modeling concept

To illustrate the proposed concept for modeling multiple propagating delamination cracks in shell elements, three numerical examples are presented. The first example concerns the simulation of a double cantilever beam (DCB) test with the purpose of validating the kinematics of the prototype element under progressive mode I delamination propagation. Similarly, in the second example the kinematical representation of the current concept is also validated for mode II delamination propagation by comparing the results obtained from FE simulations of an edge notched flexure (ENF) test to analytical results obtained using beam theory. Finally, to also illustrate the capability of the modeling concept to handle arbitrarily many delamination cracks within one and the same shell element, a cantilever beam with six delamination cracks of different size is analyzed and the results obtained are compared to analytical results with good accuracy.

In all the examples, a transversely isotropic elastic material model has been used for the mechanical response of all laminae with material parameters taken from Robinson and Song [20], reporting data for a carbon fibre

epoxy (XAS-913C). Furthermore, all laminae have a zero degree orientation to facilitate the comparison of the results obtained from the FE analyses with results obtained form analytical Euler-Bernoulli beam theory.

E_{L}	126 GPa
$E_{\mathrm{T}} = E_{\mathrm{TT}'}$	10 GPa
$G_{\mathrm{LT}} = G_{\mathrm{TT}'}$	8 GPa
$\nu_{\mathrm{LT}} = \nu_{\mathrm{TT}'}$	0.29

Table 1: Material parameters used for the numerical examples.

9.1. Progressive delamination in a double cantilever beam test

The problem consists of a beam, composed of two laminae, which has an initial delamination crack of length $a = 3$ mm, see Figure 5 for an illustration. The length of the beam is $L = 200$ mm, it has a height of $h = 3$ mm and a width of $w = 15$ mm. The beam is modeled using approximately $4,000$ triangular shell elements with quadratic approximations and has a high mesh density[5] in the region close to the delamination front. Furthermore, in the analysis the free ends of the beam are subjected to prescribed displacements in the vertical direction with a magnitude p, and the resulting reaction force R is calculated.

Since the focus of the current example is on the growth of a single delamination crack, only one set of discontinuous degrees of freedom, $\{\bar{\boldsymbol{\varphi}}_1^d,\ \boldsymbol{m}_1^{\mathrm{d}}\}$, is needed for the displacement enrichment for the nodes within the enrichment zone associated with the single delamination Γ_1. This enrichment will decouple the beam into its upper and lower laminae, which are only connected through the cohesive traction along the interface in the area with a not yet fully developed delamination crack.

In order to model the progressive growth of the delamination crack, a bilinear cohesive zone model, cf. Section 5, is used to describe the constitutive relation between the decreasing cohesive traction and the increasing crack opening displacement in the delamination progression zone. The fracture energy associated with mode I loading of the cohesive zone is set to $\mathcal{G}_{\mathrm{Ic}} = 281$ N/m – also taken from Robinson and Song [20] – and the interface strength

[5]The element edge length in the most refined area in the delamination zone of the DCB is approximately 0.35 mm.

in peel is set to $\sigma_{\text{fn}} = 57$ MPa in this example similar to what was used by Mi *et al.* [21] when analyzing the same experiment.

By analyzing the numerical results obtained from the FE analysis using the proposed modeling concept, it can be concluded that these numerical results correspond well with analytical results obtained from classical Euler-Bernoulli beam theory, cf. Figure 6. The maximum difference between the reaction forces calculated in the FE analysis and with the analytical theory is less than 0.6 % for any given prescribed displacement p (during delamination propagation).

It should also be remarked that the discrepancy in results during elastic loading is due to the fact that in order to obtain the analytical results, it is assumed that the beam is clamped at the crack tip with zero rotation of the cross section. This is obviously not the case in the FE analysis leading to a softer response in this stage of the analysis compared to the analytical beam solution. However, since the main focus of this example is to validate the progressing delamination, in which stage there is a good correspondence, we can conclude that the proposed modeling concept is suitable for accurately representing progressive delamination propagation in mode I.

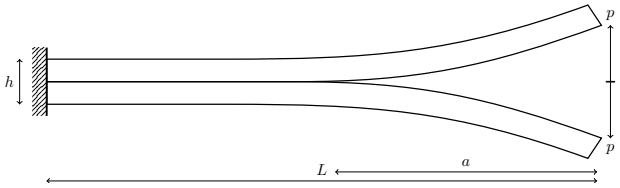

Figure 5: Geometry of the DCB test used in the example in Subsection 9.1. The free ends are displaced a distance p.

9.2. Progressive delamination in an edge notch flexure test

In the second example, we study the predictive capability of the modeling concept for mode II crack propagation. For this purpose, an ENF test is analyzed where the beam considered is, as in the previous example, a two laminae beam with the same geometric dimensions. It has an initial delamination crack of length $a = 80$ mm and is simply supported, see Figure 7 for an illustration. The beam is modeled using $1,300$ quadratic triangular elements with an increased mesh density in the region close to the delami-

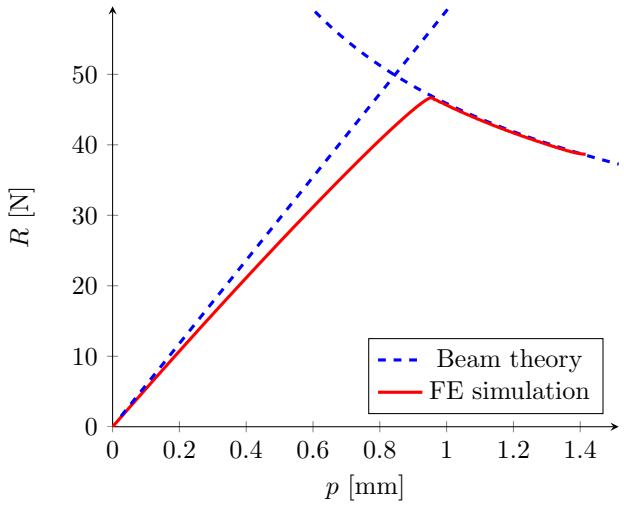

Figure 6: Comparison of calculated reaction force R (FE analysis and analytical beam theory) versus prescribed end point displacement p for the DCB example in Subsection 9.1.

nation front[6]. Furthermore, during the simulation the mid-surface is at $L/2$ subjected to a increasing prescribed displacement p in the vertical direction and the resulting reaction force R is calculated.

The same bilinear cohesive zone model as in the previous example is used to describe the constitutive relation between the decreasing cohesive traction and the increasing crack sliding (mainly) displacement in the delamination progression zone. For this example, the fracture energy associated with mode II loading of the cohesive zone is set to $\mathcal{G}_{\mathrm{IIc}} = 800$ N/m and the interface strength in shear is set to $\sigma_{\mathrm{fs}} = 100$ MPa.

Just as for the mode I case, it can be concluded that the numerical results obtained from the FE analysis of a propagating mode II crack using the proposed modeling concept correspond well with analytical results obtained from classical Euler-Bernoulli beam theory, cf. Figure 8. The maximum difference between the reaction forces calculated in the FE analysis and with the analytical theory is less than 2.5 % for any given prescribed displacement p.

There is a slight discrepancy in the FE and analytical results. This can

[6]The element edge length in the most refined area in the delamination zone of the ENF is approximately 0.75 mm.

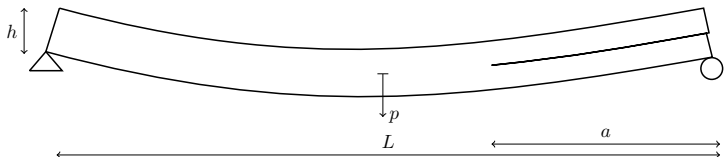

Figure 7: Geometry of the ENF beam used in the example in Subsection 9.2. The middle of the beam is displaced the distance p.

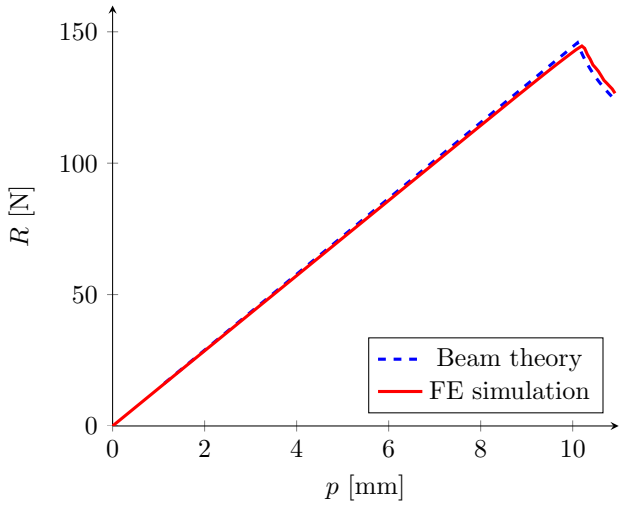

Figure 8: Comparison of calculated reaction forces R (FE analysis and analytical beam theory) versus prescribed midpoint displacement p for the ENF example in Subsection 9.2.

be explained by the fact that in the analytical solution, no interpenetration is assumed between the laminae, whereas in the FE analysis, some interpenetration is unavoidable due to the finite compressive stiffness of the cohesive zone model which will also translate into a somewhat weaker response of the beam. This in turn leads to a slight delay in the initial propagation of the crack. However, the difference is small and not a direct consequence of the current modeling concept, but rather an inherent effect of using a penalty approach to avoid interpenetration. Therefore, we can conclude that the proposed modeling concept is suitable for accurately representing progressive delamination propagation also in mode II.

9.3. Cantilever beam with multiple delaminations

In the first two examples, the proposed modeling concept has only been tested for one interlaminar crack. Therefore, there is a need to also demon-

strate the capabilities of the concept to handle multiple delaminations within one and the same shell element. For this purpose, we again consider the geometrical setup in the two previous examples but with the difference that the beam now is composed of seven laminae. In the beam, there are six interlaminar cracks of different size (length), the length of which is parameterized in terms of the length of the shortest crack $a = 30$ mm, cf. Figure 9 for details. The reader should note that, elements closest to the free edge will thus have six active enrichments while the elements closest to the wall will have none. Furthermore, the beam is modeled using 80 quadratic triangular elements with an approximate element size of 7.5 mm. Finally, the beam is subjected to a constant edge load t at the top of the beam (at its free end) with the magnitude 10 N/m in the vertical direction.

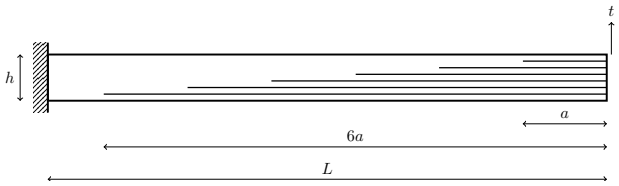

Figure 9: Geometry of the beam with multiple (6) interlaminar cracks of different length considered in the example in Subsection 9.3. A vertical traction $\boldsymbol{t}$ is applied on the upper edge.

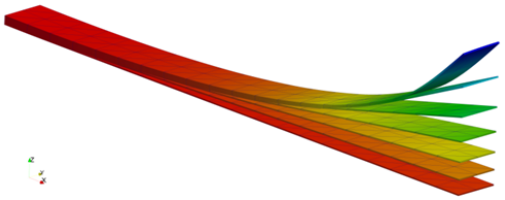

Figure 10: Displacement field for beam with multiple delamination cracks (magnification factor = 50) considered in the example in Subsection 9.3

In Figure 10, the deformation pattern obtained from the FE analysis of the beam is shown in perspective illustrating that a shell element enriched according to the proposed modeling concept can handle multiple delaminations. More specifically, by comparing the results obtained in the FE analysis to (again) Euler-Bernoulli beam theory, it is concluded that the difference in calculated maximum beam deflection is less than 0.5 %. In addition, from

Figure 11, where the resulting deformation pattern from the FE analysis (continuous surface) is compared to the deformation pattern obtained from beam theory (black squares), it can be directly seen that the obtained overall solution corresponds well with beam theory. Thus, not only the maximum deflection is predicted with good accuracy, but the total deformation of the beam is predicted well.

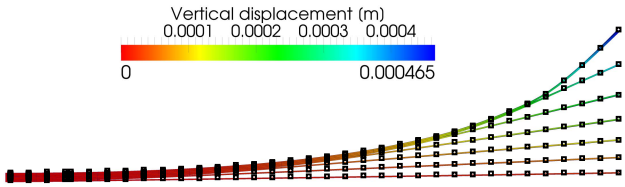

Figure 11: Comparison of FE solution with beam theory for the multiple delamination example in Subsection 9.3, where the shell results are overlayed by the analytical results (squares) based on Euler - Bernoulli theory, showing good agreement.

10. Summary and conclusions

In this paper, we propose a generic concept for the modeling of multiple and arbitrarily located interlaminar cracks in a (potentially curved) laminate. In this context, we acknowledge parallel (to this paper) developments presented in the literature based on isogeometric analysis, which shows good potential in modeling arbitrary delaminations in shells (for *e.g.* composites), cf. Hoseini *et al.* [22]. However, since the focus has been to develop a concept which can be incorporated within a traditional finite element framework, we have based the current concept on the eXtended Finite Element Method.

The proposed concept is an extension of previously reported works on the modeling of a single, but arbitrarily located interlaminar crack, by Larsson [13] and de Borst and Remmers [14]. Similarly to what is proposed therein, the current modeling concept is based on the XFEM whereby one main benefit is that propagating delamination cracks can be kinematically represented independently of the spatial discretizations (the finite element mesh) in the FE analysis. Hence, the kinematical representation of the laminate can be adaptively and automatically refined (enriched) whenever a new crack initiates or an existing crack propagates, such that any number of interlaminar cracks can be realized. The realization of these multiple delaminations is achieved independently of the initial spatial representation, which

then can be rather coarse. As a consequence, a structural model of a thin-walled laminate can, by using this modeling concept, initially be built up by a single layer of shell elements through the thickness whereby also the model preparation is simplified. During loading, the model is then enriched locally in critical areas where delamination is predicted.

To be precise, the proposed modeling concept has the potential of leading to increased computational efficiency due to two key aspects:

- the shell formulation only involves a local enrichment of the displacements in the vicinity of the delamination crack(s) leaving the remaining structure unaffected and
- enrichments do not need to be added *a priori* but is dynamically introduced when and where delaminations develop

– indeed these aspects lie at the heart of the proposed modeling concept.

These points means that additionally introduced degrees of freedom are kept to a minimum since they are added in relation to the size and number of delaminations cracks and their evolution. Thereby, the computational cost is reduced compared to the more traditional approach based on, for example, stacked shell elements interconnected with cohesive elements which results in a high number of degrees of freedom even for an undamaged structure.

To illustrate the proposed concept, it has been applied to a specific shell element formulation in line with previous developments to model through-thickness crack propagation in thinwalled structures [18]. However, we would like to stress that the formulation is more general and can easily be applied other shell formulations as well as solid element formulations.

In the example section of the paper, the resulting shell element has been verified for propagation in pure deformation modes (I and II), as well as for stationary loading involving multiple delaminations. Based on the results presented in this paper, we conclude that the proposed modeling concept is suitable for simulation of thinwalled structures undergoing substantial delaminations. In particular for applications where computationally efficiency is of major importance, such as car crash analyses.

Acknowledgements

The research leading to these results receives funding from the European Communitys Seventh Framework Programme (FP7/2007-2013) under grant

agreement no. 314182 (the MATISSE project). This publication solely reflects the authors views. The European Community is not liable for any use that may be made of the information contained herein. In addition, funding from the strategic innovation programme LIGHTer provided by VINNOVA is also acknowledged.

References

[1] J.J. Carruthers, A.P. Kettle, and A.M. Robinson. Energy absorption capability and crashworthiness of composite material structures: A review. *Appl. Mech. Rev.*, 51:635–649, 1998.

[2] G.C. Jacob, J.F. Fellers, S. Simunovic, and J.M. Starbuck. Energy absorption in polymer composites for automotive crashworthiness. *J. Compos. Mater.*, 36:813–850, 2002.

[3] H. Hamada, J.C. Coppola, D. Hull, Z. Maekawa, and H. Sato. Comparison of energy absorption of carbon/epoxy and carbon/peek composite tubes. *Composites*, 23:245–252, 1991.

[4] D. Hull. A unified approach to progressive crushing of fibre-reinforced composite tubes. *Compos. Sci. Technol.*, 40:377–421, 1991.

[5] L. Grauers, R. Olsson, and R. Gutkin. Energy absorption and damage mechanisms in progressive crushing of corrugated NCF laminates: Fractographic analysis. *Compos. Struct.*, 110:110 – 117, 2014.

[6] P. Feraboli. LS-DYNA MAT54 modeling of the axial crushing of a composite tape sinusoidal specimen. *Compos. Part A–Appl. S.*, 42:1809–1825, 2011.

[7] B.P. Bussadori, K. Schuffenhauer, and A. Scattina. Modelling of CFRP crushing structures in explicit crash analysis. *Compos. Part B–Eng.*, 60:725–735, 2014.

[8] L. Greve and A.K. Pickett. Delamination testing and modelling for composite crash simulation. *Compos. Sci. Technol.*, 66:816–826, 2006.

[9] T. Belytschko and T. Black. Elastic crack growth in finite elements with minimal remeshing. *Int. J. Numer. Meth. Eng.*, 45:601–620, 1999.

[10] N. Moës, J. Dolbow, and T. Belytschko. A finite element method for crack growth without remeshing. *Int. J. Numer. Meth. Eng.*, 46:131–150, 1999.

[11] F.P. van der Meer, L.J. Sluys, S.R Hallett, and M.R Wisnom. Computational modeling of complex failure mechanisms in laminates. *J. Compos. Mater.*, 46:603–623, 2011.

[12] A. Ahmed, F. van der Meer, and L.J. Sluys. A geometrically nonlinear discontinuous solid-like shell element (DSLS) for thin shell structures. *Comput. Method Appl. M.*, 201-204:191–207, 2012.

[13] R. Larsson. A discontinuous shell-interface element for delamination analysis of laminated compos. struct. *Comput. Method Appl. M.*, 193:3173–3194, 2004.

[14] R. de Borst and J.J.C. Remmers. Computational modelling of delamination. *Compos. Sci. Technol.*, 66:713–722, 2006.

[15] R.C. Batra and J. Xiao. Analysis of post-buckling and delamination in laminated composite st. venant–kirchhoff beams using CZM and layerwise TSNDT. *Compos. Struct.*, 105:369–384, 2013.

[16] J. Brouzoulis and M. Fagerström. Modelling of multiple delaminations in shells using XFEM. In *Proc. 19th Int. Conf. Composite Materials*. 2013.

[17] M. Fagerström and R. Larsson. Approaches to dynamic fracture modelling at finite deformations. *J. Mech. Phys. Solids*, 56:613–639, 2008.

[18] R. Larsson, J. Mediavilla, and M. Fagerström. Dynamic fracture modeling in shell structures based on XFEM. *Int. J. Numer. Meth. Eng.*, 86:499–527, 2010.

[19] R. Hauptmann, S. Doll, M. Harnau, and K. Schweizerhof. 'Solid-shell' elements with linear and quadratic shape functions at large deformations with nearly incompressible materials. *Comput. Struct.*, 79:1671–1685, 2001.

[20] P. Robinson and D.Q. Song. A modified DCB specimen for mode I testing of multidirectional laminates. *J. Compos. Mater.*, 26:1554–1577, 1992.

[21] Y. Mi, M.A. Crisfield G.A.O. Davies, and H.B. Hellweg. Progressive Delamination Using Interface Elements. *J. Compos. Mater.*, 32:1246–1272, 1998.

[22] S. Hosseini, J.J.C. Remmers, C.V. Verhoosel, and R. de Borst. An isogeometric continuum shell element for non-linear analysis. *Comput. Method Appl. M.*, 271:1–22, 2014.